Design of a 4.8-m ring for inverse Compton scattering x-ray source

H. S. Xu,[1,2,*] W. H. Huang,[1,2] C. X. Tang,[1,2] and S. Y. Lee[3]

[1]*Accelerator Laboratory, Department of Engineering Physics, Tsinghua University, Beijing 100084, China*

[2]*Key Laboratory of Particle and Radiation Imaging (Tsinghua University), Ministry of Education, Beijing 100084, China*

[3]*Department of Physics, Indiana University, Bloomington, Indiana 47405, USA*

(Received 7 December 2013; published 10 July 2014)

In this paper we present the design of a 50 MeV compact electron storage ring with 4.8-meter circumference for the Tsinghua Thomson scattering x-ray source. The ring consists of four dipole magnets with properly adjusted bending radii and edge angles for both horizontal and vertical focusing, and a pair of quadrupole magnets used to adjust the horizontal damping partition number. We find that the dynamic aperture of compact storage rings depends essentially on the intrinsic nonlinearity of the dipole magnets with small bending radius. Hamiltonian dynamics is found to agree well with results from numerical particle tracking. We develop a self-consistent method to estimate the equilibrium beam parameters in the presence of the intrabeam scattering, synchrotron radiation damping, quantum excitation, and residual gas scattering. We also optimize the rf parameters for achieving a maximum x-ray flux.

DOI: 10.1103/PhysRevSTAB.17.070101 PACS numbers: 29.20.D-, 41.85.Ar, 41.85.Gy

I. INTRODUCTION

Inverse Compton scattering (ICS) between high power infrared laser and medium energy electron beams is a promising source of intense tunable x rays for various applications [1,2]. The maximum energy of the scattered photons in the head-on collision is $E_{X,\max} = 4\gamma^2 E_L$, where γ is the initial Lorentz factor of the electron beam and E_L is the photon energy in the incident laser. For instance, the ICS between 50 MeV electrons and 800 nm laser can produce hard x-ray photons up to 59 keV. However, the cross section of ICS is small [3] and thus the total x-ray flux is low. Huang and Ruth proposed a scheme for an ICS x-ray source [4], in which electron beams are stored in a compact ring, while laser pulses are stored in an optical cavity. In this scheme, the repetition frequency of the laser-electron interaction is determined by the revolution frequency of the electron beam in the compact ring, of the order of tens of MHz.

There are two operational schemes for the ICS x-ray sources consisting mainly of linacs, compact rings and optical cavities. The first is called pulsed mode [4–8], in which the stored electron beams are refreshed before achieving equilibrium. In the energy range around tens of MeV, the synchrotron radiation damping is weak [9]. On the other hand, the intrabeam scattering (IBS) effect dominates [10,11]. The emittances of the electron beams may increase after injection. Refreshing the electron beams frequently is effective in producing higher x-ray flux by keeping higher brightness electron beams in the rings. Thus, the pulsed mode takes advantage of the high beam quality of the linac source. Unfortunately, the flux of x-ray photons reduces continuously in one storage period as the laser pulse interacts with the continually diffusing electron beam [6]. Furthermore, this mode of operation suffers from the pulse-by-pulse jitter of the linac. The x-ray flux may fluctuate due to the jitter of the injected electron beams.

Another operational mode is the steady-state mode [12–14], in which steady x-ray flux can be produced because the state of equilibrium of the electron beams has been reached. A storage ring, with optimized beam lifetime, is required in this mode.

There are several compact ring based ICS x-ray sources currently in commissioning, or under construction. The compact light source (CLS) [15], designed by the Lyncean Technologies Inc., is operated only in the pulsed mode. A single electron bunch circulates for about one million turns in the ring of CLS before being dumped. It succeeds in producing photons over 10 keV by storing about 25 MeV electron beams in the ring [8]. The NESTOR project [16,17] and ThomX project [18] are proposed to have the capability of running in both pulsed mode and steady-state mode. The NESTOR ring, which is in commissioning [19,20], has 15.4 meter circumference. The energy of stored beams is tunable for producing scattered photons from x ray up to γ ray. The ThomX project, which is under construction, consists of a 50 MeV electron injector, a 16.8 meter ring and a 2 D Fabry-Perot cavity.

This paper presents a design of a compact ring for the Tsinghua Thomson scattering x-ray source (TTX) [21]. Our

*xhs05@mails.tsinghua.edu.cn

goal is to design a compact ring and retain the capability of both pulsed mode and steady-state mode operation. We propose to use four dipole magnets with small bending radius and nonzero edge angles to provide both horizontal and vertical focusing. We find that a 4.8 meter storage ring provides satisfactory beam dynamics for the TTX, including dynamic aperture, momentum aperture, error analysis, intrabeam scattering, space charge effects, and rf beam dynamics. We organize this paper as follows. Section II discusses the design of basic optics of a compact ring, including lattice structure, dynamic aperture, and injection scheme. Section III studies the nonlinear beam dynamics induced by bending magnets with small bending radius, and multiparticle effects on equilibrium beam properties. The intrinsic geometric nonlinearity induced by the dipole magnets with small bending radius is studied via both the analytical approach and particle tracking. On the multiparticle effects, we develop a two-stage self-consistent method to estimate the emittances' evolution process of a beam, in the presence of strong intrabeam scattering (IBS), synchrotron radiation damping, quantum excitation, and residual gas scattering. Section IV shows the optimization of the rf parameters and Touschek lifetime. The conclusion is given in Sec. V.

II. BASIC DESIGN

A. Basic optics

We propose a four-dipole lattice for the TTX electron storage ring. Both length and edge angle of the dipole magnets are optimized in order to provide proper horizontal and vertical focusing. Figure 1 shows the tune diagram of "stable" solutions, with superperiodicity of 2, circumference of 4.8 m, and lengths of the short and long straights of 0.5 and 1.1 m respectively. In these calculations, we have included the fringe field effect of the dipole magnets, which can affect the betatron tunes in low energy synchrotrons [22]. We use the Karl L. Brown's formalism [23], where the vertical gap g and the fringe field integral (FINT) value are used to describe the fringe field effect:

$$\mathrm{FINT} = \int_{-\infty}^{+\infty} \frac{B_z(s)[B_0 - B_z(s)]}{gB_0^2}\, ds, \qquad (1)$$

where $B_z(s)$ is the magnitude of the fringe field on the magnetic midplane at a position s. B_0 is the designed magnitude of the magnetic induction intensity in the main body of the dipole magnets. No exact FINT value can be obtained before the measurement of the real magnets. However, through the study of the FINT value of the common benders at PSR in Los Alamos National Laboratory, we choose FINT $= 0.9$ [24] and choose magnet gap of $g = 2.54$ cm in our baseline design.

In electron storage rings, quantum fluctuation can cause particle diffusion. The horizontal damping partition number

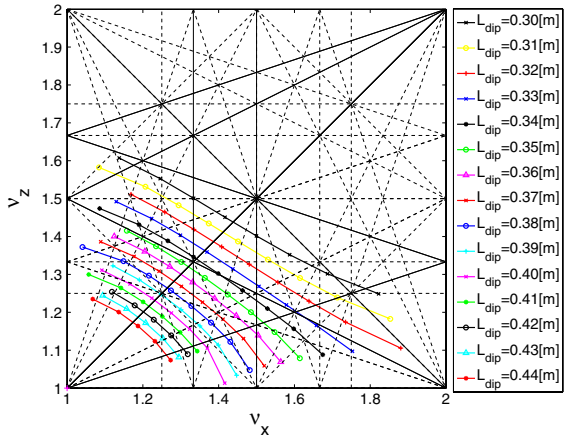

FIG. 1. Tune diagram for various lengths and edge angles of dipole magnets. The bare lattice consists of four dipoles with edge angles. Each curve (same color and symbol) corresponds to dipole length from 0.31 to 0.44 m, respectively. On each curve, different data points correspond to different edge angles of the same dipole length, where the edge angle varies by an increment of 1°.

$\mathcal{J}_x$ is typically negative in the rings with dipole magnets only, even though the edge angles of dipole magnets provide small positive contribution. A positive $\mathcal{J}_x$ is necessary for particles to achieve damping from synchrotron radiation. We propose to place two quadrupoles at the centers of the two opposite long straight sections to adjust $\mathcal{J}_x$.

The betatron tunes and $\mathcal{J}_x$ depend on dipole length, edge angle, and the quadrupole strength. Figure 2 shows the tune diagram for dipole length of 0.40 m with various edge angles and quadrupole strengths, indicated by different symbols and different colors respectively. Based on this analysis, we can choose proper edge angles and quadrupole strengths to avoid harmful low order systematic resonance lines. Figure 3 shows the horizontal damping partition number vs edge angle and quadrupole strength.

In this optimization process, we choose the canonical design with parameters as (1) the length of each dipole magnet 0.4 meter, where the corresponding bending radius is about 0.2546 meter and (2) edge angle of 37°. This choice is made after considerable research on the intrinsic nonlinear effects induced by the geometric nonlinearity in dipole magnets which is to be discussed in Sec. III A.

Figure 3 shows that the horizontal damping partition number $\mathcal{J}_x$ varies from 0.4 to 1.5 as the strength of quadrupoles changes from 10 to 40 m^{-2}. When quadrupole strength is 30 m^{-2}, the lattice is a double-bend achromat, i.e. the dispersion function at the IP and cavity straight section is zero. Figure 4 shows the baseline optics, of which the betatron tunes are $\nu_x = 1.21$, and $\nu_z = 1.28$.

The momentum compaction factor α_c also changes when the quadrupole strength changes. For example, in the above lattice, α_c varies from about 1.1 to -0.5 vs quadrupole

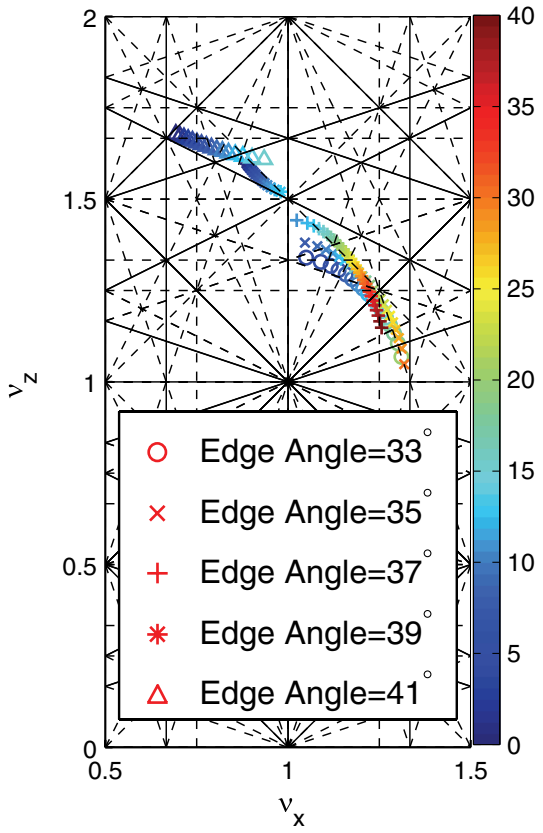

FIG. 2. Tune diagram for various edge angles of dipole magnets and quadrupole focusing strengths in units of m^{-2}. Four 90° dipole magnets of length 0.40 m each, and two 10-cm quadrupoles located at the centers of the long straight sections are included in the calculation. Different types of markers stand for edge angles of dipole magnets. The color bar indicates focusing strengths of the quadrupoles.

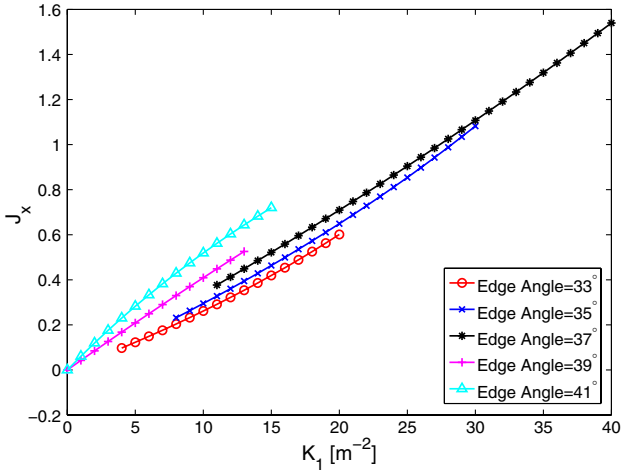

FIG. 3. Horizontal damping partition number $\mathcal{J}_x$ vs quadrupole focusing strengths and various edge angles of the dipole magnets. The focusing strengths of quadrupoles K_1 vary within the stable condition.

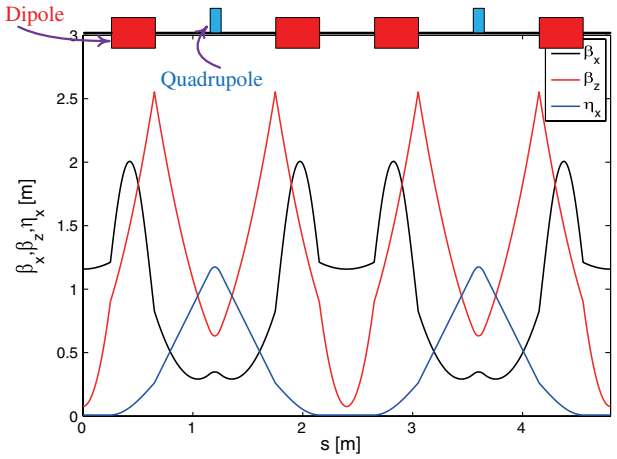

FIG. 4. The layout, betatron amplitude functions and dispersion function of the baseline design of the 4.8-m ring. The length of each dipole magnet is 0.4 m with bending angle 90°. The edge angles at both the entry and the exit of each dipole magnet are 37°. We consider iron magnet with 2.54 cm vertical gap. The first order fringe field effect is included with the FINT parameter of 0.9. The quadrupole focusing strength K_1 is 30 m^{-2}.

strengths from 10 to 40 m^{-2}. The momentum compaction factor is tunable, which gives us opportunity to study the beam dynamics under isochronous condition, and lattice with negative momentum compaction factor, etc. In the baseline design, α_c is around 0.13.

B. Dynamic aperture

Dynamic aperture (DA) is defined as the maximum amplitude of stable particle motion [25]. Large dynamic aperture is required for the purpose of avoiding loss of particles with large actions. Typically, sextupoles are used to increase DA for both on-momentum particles and off-momentum particles by correcting chromatic aberration and compensating geometric aberration.

The natural chromaticities of the baseline lattice are about −2.1 and −1.0 in horizontal and vertical directions, respectively. The tune shift for particles with ±3.0% momentum deviation are about ∓0.06 and ∓0.03 in the horizontal and vertical planes. Therefore, the tune spread of a beam with a reasonable momentum spread will not encounter systematic integer, half integer or third order resonance lines in the baseline design. We believe that sextupoles are not necessary in this 4.8 m ring. Moreover, based on the current state of knowledge [26], the head-tail instability can be controlled without using any sextupole because the momentum compaction factor is tunable from a positive value to a slightly negative one [27]. However, the criterion of this instability in such kind of low energy compact rings is still worthwhile exploring in the future. This ring gives us an opportunity to study this topic.

The calculation of DA is based on particle tracking. After careful analysis, we find that DA reaches convergence

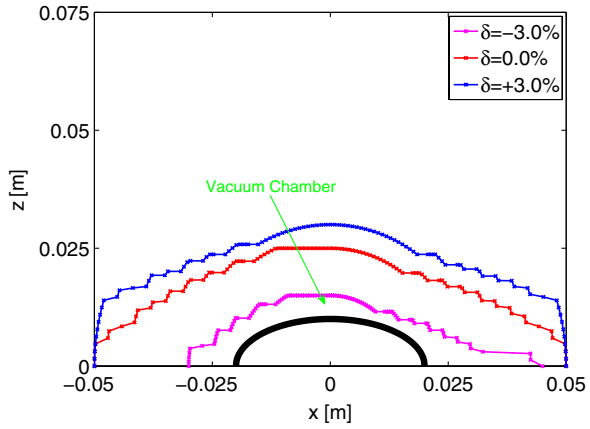

FIG. 5. The dynamic aperture at the center of one of the short straight sections for the particles with three different momentums. The black half-ellipse shows the cross section of the vacuum chamber at this position.

when the particles are tracked for more than 20000 turns. Figure 5 shows the 20000-turn DA at the IP for on-momentum particles and particles with ±3.0% momentum deviation. The dynamic apertures in the three cases are all larger than the effective vacuum chamber.

However, 20000 turns may not be enough for studying the long term behavior of particles. For example, in the pulsed mode, an electron bunch will be stored in the ring for about 10 ms, or 6×10^5 turns. To track so many turns in the study of dynamic aperture is time consuming. We therefore turn to frequency map analysis (FMA), which can provide a prediction of the long term diffusion rate [28]. The FMA is therefore a supplement of the study of dynamic aperture. ELEGANT code [29] is used to perform FMA. Figure 6 shows the FMA results for the on-momentum

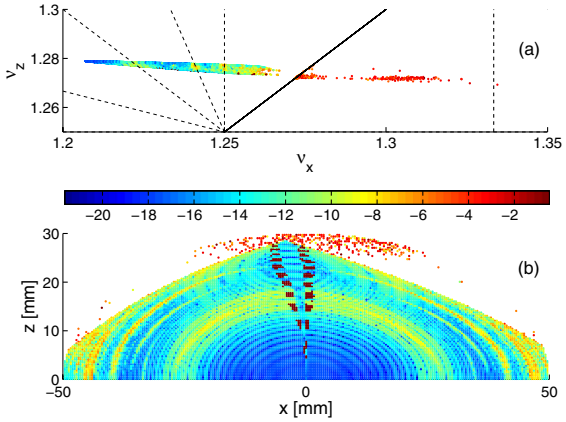

FIG. 6. The frequency map for on-momentum particles of the ideal lattice of the 4.8-m ring. Particles are initially uniformly distributed in the transverse plane. Plot (b) shows the survived particles. The betatron tunes of each survived particle are plotted in the tune space shown in plot (a). The color bar indicates the tune diffusion rates. Particles with smaller diffusion rate are more stable. Some low order resonances are shown on the top plot.

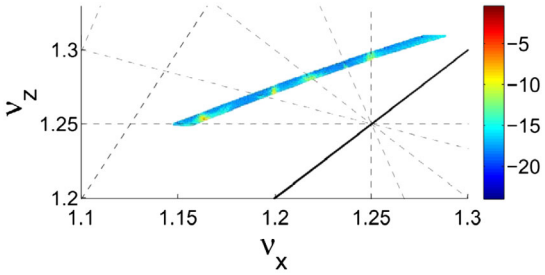

FIG. 7. The tune footprint of particles uniformly distributed in the effective vacuum chamber. The momentum spread is set between $\delta_p = -3.0\%$ and $+3.0\%$. The color bar stands for the tune diffusion rate, defined as $\log_{10}(\Delta\nu_x^2 + \Delta\nu_y^2)$. There is no particle loss in the tracking. Both tune spread and diffusion rate are small.

particles in an ideal lattice. The cross section of the survived particles, whose colors indicate the diffusion rate, is shown in the lower plot. Meanwhile, the tune spread of the corresponding particles is shown in the upper one. The boundary of the stable area shown in Fig. 6(b) is the same as the one shown in Fig. 5. Figure 6(a) shows the small tune spread and low diffusion rate for particles near the center of the DA, which indicates that the particles are very stable.

FMA is also used to study the stability of the particles varying momentum deviation from $\delta_p = -3.0\%$ to $+3.0\%$ within the effective vacuum chamber (shown in Fig. 5). The tune footprint of this study is shown in Fig. 7, which verifies low diffusion rate for all particles. Moreover, no low order systematic resonance lines (lower than the fourth order) are crossed, which implies the fact that the particles with continuous varying momentum from $\delta_p = -3.0\%$ to $+3.0\%$ within the effective vacuum chamber are stable. The results of the FMA are consistent with the DA particle tracking.

C. Injection system

The 4.8 m ring is designed to operate in both pulsed mode and steady-state mode. In the steady-state mode, the equilibrium beam parameters are used in x-rays production. High injection efficiency is the main requirement in this case. However, in the pulsed mode, the electron beam interacts with laser pulse immediately after injection. Any jitter in the electron beam orbit will induce coherent betatron oscillation, which leads to flux fluctuation of the x-ray photons. Due to the weak synchrotron radiation damping in this ring, the initial coherent betatron oscillation is difficult to be damped. Thus we propose an on-axis injection scheme for the pulsed mode. To simplify the process, we propose to put the linac and the ring at the same vertical height in order to remove the initial vertical motion. The injection process can be described in the horizontal phase space instead of the 4D transverse phase space. A horizontal kicker is required to provide horizontal injection. Figure 8 illustrates the injection process in both real space

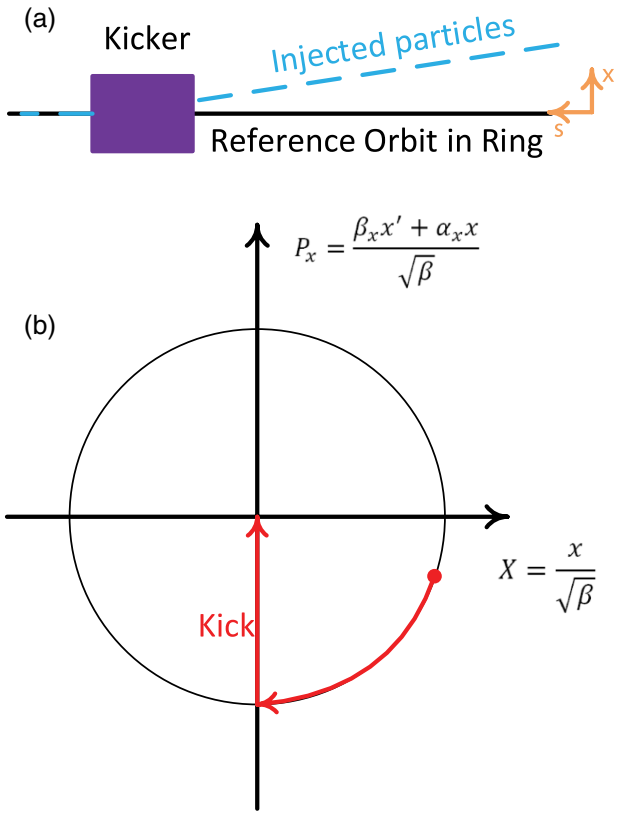

FIG. 8. Schematic drawing of the on-axis injection process. The top plot (a) shows the top view of the horizontal-longitudinal plane (x, s), illustrating the designed injection process in real space. The bottom plot (b) shows the injected beam moves along the circle in the normalized horizontal phase space (X, P_x) before it is kicked to the center by a kicker.

and horizontal normalized phase space schematically. In the process, the injected particles move towards the reference orbit with a small angle before passing through a kicker, and then the particles are kicked to the center of phase space. However, in the optimization of the injection process, we consider a finite length kicker, which can remove not only the small angle but also the small residual displacement.

We use the fringe field of the dipole magnet located upstream the kicker to provide extra bend to the injected beam, as shown schematically in Fig. 9. The injected beam will pass through the quadrupole Q1 at off-center positions. The dipole field component of the Q1 should also be considered in the design of the injection system. The design strategy of the injection scheme in this ring is discussed in detail in [30]. In this paper, we use the CST EM STUDIO [31] to simulate the 3D magnetic field of the upstream dipole magnet and the quadrupole magnet. The trajectory of the injected beam is obtained by solving the equations of motion in 3D magnetic field via the fourth order Runge-Kutta method [32]. The optimized trajectory of the centroid of the injected beam is shown by the cyan curve in Fig. 10.

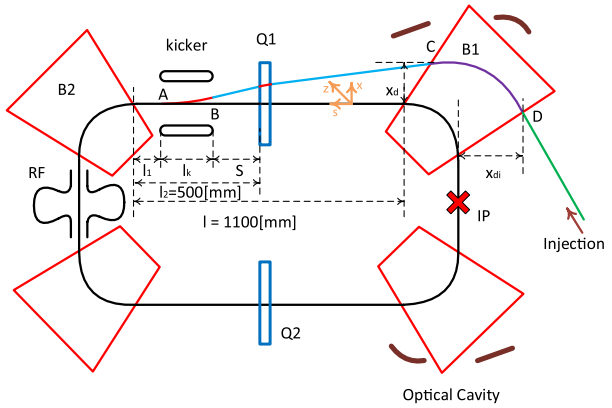

FIG. 9. Schematic top view of the injection system in the 4.8 m ring. The injected beams enter the fringe field region of the dipole magnet B1 at the point D, and then, leave B1 at point C. x_{di} and x_d indicate the horizontal coordinates of point C and D in the Frenet-Serret coordinate system, which is expressed as (x, z, s) in this figure (z axis is perpendicular to the paper), respectively. l_1, S, and l_2 illustrate the location of the kicker. l_k is the length of the kicker. The injected beams pass through the quadrupole magnet Q1 before entering into the kicker. The rf cavity and the interaction point (IP) are located at the center of the short straight sections.

The injected particle moves from right to left, passing through the fringe field region of the dipole magnet and the quadrupole. The optimum distance and divergence between the central trajectory of the injected beam and the reference orbit in the ring are about 24.8 mm and 97.8 mrad at the

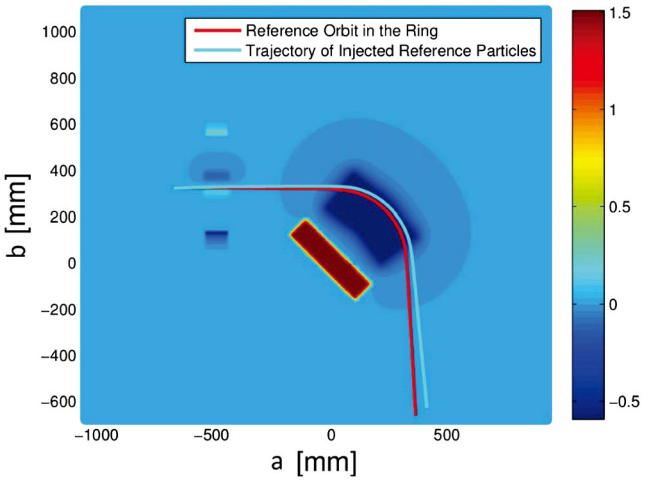

FIG. 10. Injection trajectory in the central (x, s) plane at $z = 0$. The Cartesian coordinates (a, b) in the central plane are used to present the simulated magnetic field. The injection trajectory and the reference orbit are respectively shown in cyan and red curves. The color bar means the value of magnetic field B_y. The injected particles move from right to the left, passing through the fringe field region of the dipole magnet and the quadrupole. The left end of the two trajectory is the entry of the kicker which corresponds to the point B shown in Fig. 9. The optimum x_B and x'_B are 4.9 mm and 28 mrad, respectively.

TABLE I. Parameters of the injection system.

Parameters	Values
Peak voltage of the kicker [kV]	30
Distance between the two striplines [mm]	30
l_1 [mm]	100
Length of the kicker l_k [mm]	350
S [mm]	50
x_d [mm]	12.7
x'_d [mrad]	9
x_{di} [mm]	24.8
x'_{di} [mrad]	97.8

entrance of the dipole magnet, respectively. Table I lists the main parameters in the baseline design of the injection scheme.

In the injection process, if the beam receives residual kick after a single pass, coherent betatron oscillation of the whole beam will be excited. Since the revolution period of the stored beam is about 16 ns, the rise and fall time of the conventional ferrite kicker with thyratron switch is too long. To overcome this difficulty, we propose a traveling wave kicker system which is usually the preferable way to generate ultrashort field pulse for injection and extraction [33,34]. The effect of electric and magnetic fields adds up together to gain a factor of 2 in the kicker strength if the traveling wave counterpropagates to the direction of electron beams.

III. BEAM DYNAMICS

A. Intrinsic nonlinearity of the bending magnets

The geometrical nonlinear effect induced by the dipole magnets is usually ignored in the design of high energy ring lattice. However, it becomes significant when the bending radius is small. The intrinsic nonlinearity of dipole magnets can be described by the Hamiltonian in Frenet-Serret coordinate system [25],

$$\tilde{H} = -\left(1+\frac{x}{\rho}\right)\left[\frac{(H-e\Phi)^2}{c^2} - m^2c^2 - (p_x - eA_x)^2 - (p_z - eA_z)^2\right]^{1/2} - eA_s, \tag{2}$$

where the phase-space coordinates are $(x, p_x, z, p_z, t, -H)$. The total energy and momentum of the particle are $E = H - e\Phi$ and $p = \sqrt{E^2/c^2 - m^2c^2}$. Since the transverse conjugate momenta p_x and p_z are much smaller than the total momentum, we expand the Hamiltonian up to second order in p_x and p_z:

$$\tilde{H} \approx -p\left(1+\frac{x}{\rho}\right) + \frac{1+x/\rho}{2p}[(p_x - eA_x)^2 + (p_z - eA_z)^2] - eA_s. \tag{3}$$

The betatron equations of motion become

$$x'' - \frac{\rho + x}{\rho^2} = -\frac{B_z}{[B\rho]}\frac{p_0}{p}\left(1+\frac{x}{\rho}\right)^2,$$
$$z'' = +\frac{B_x}{[B\rho]}\frac{p_0}{p}\left(1+\frac{x}{\rho}\right)^2, \tag{4}$$

where the $[B\rho]$ is the magnetic rigidity of the reference particles.

We consider an on-momentum particle with $p = p_0$ in dipole and quadrupole fields:

$$B_z = B_0 + \frac{\partial B_z}{\partial x}x = B_0 + B_1 x,$$
$$B_x = \frac{\partial B_z}{\partial x} = B_1 z. \tag{5}$$

The equations of motion are

$$x'' + K_x x = -\left(\frac{1}{\rho^3} + \frac{2B_1}{[B\rho]\rho}\right)x^2 - \frac{B_1}{[B\rho]\rho^2}x^3,$$
$$z'' + K_z z = \frac{2B_1}{[B\rho]\rho}zx + \frac{B_1}{[B\rho]\rho^2}zx^2, \tag{6}$$

where $K_x = 1/\rho^2 + K_1 = 1/\rho^2 + B_1/[B\rho]$, and $K_z = -K_1 = -B_1/[B\rho]$. In a dipole field region, the equations of motion become

$$x'' + K_x x = -\frac{x^2}{\rho^3},$$
$$z'' + K_z z = 0, \tag{7}$$

where the corresponding pseudo-Hamiltonian becomes

$$H = \frac{1}{2}[x'^2 + K_x x^2 + z'^2 + K_z z^2] + \frac{x^3}{3\rho^3}. \tag{8}$$

Carrying out the Floquet transformation to action-angle coordinates, the Hamiltonian becomes

$$H = \nu_x J_x + \nu_z J_z + \sum_{\ell} G_{3,0,\ell} J_x^{3/2} \cos(3\phi - \ell\theta + \xi_{3,0,\ell}) + \cdots, \tag{9}$$

where

$$G_{3,0,\ell} e^{j\xi_{3,0,\ell}} = \frac{\sqrt{2}}{12\pi}\oint \frac{1}{\rho^3}\beta_x^{3/2} e^{j[3\chi_x(s) - (3\nu_x - \ell)\theta]} ds. \tag{10}$$

The term x^2/ρ^3 in Eq. (7) is the nonlinear term introduced by the dipole magnets. This term is usually negligible unless the bending radius becomes small. The Hamiltonian shown in Eq. (9) and the resonance strength

shown in Eq. (10) indicate that the dipole field can drive the $3\nu_x =$ integer resonances at a small bending radius. Moreover, by applying the canonical perturbation method [25], we can predict that the fourth order resonances can also be driven by the dipole magnets with small bending radii.

We demonstrate this effect by tracking particles with different initial positions in the horizontal phase space (x, x'). ELEGANT code [29] is used to perform the particle tracking. Effects of both the edge angle and fringe field in dipoles are included in the tracking. There is no fringe field effect of quadrupoles included. We placed the bare horizontal tune of the particles near the center of phase space closed to the predicted third order resonance line $3\nu_x = 4$ and fourth order one $4\nu_x = 6$, respectively. Particles are tracked for 20000 turns. The Poincaré surface of section is taken for all the particles at each revolution. Figure 11(a) shows that the topology of the phase space maps are more distorted for the particles closer to the separatrix when the betatron tune of the central particles is near $3\nu_x = 4$ resonance. The triangular topology of the separatrix indicates that the third order resonance does happen. Furthermore, three islands are observed in Fig. 11(a) which are generated by the nonzero nonlinear detuning parameters. Plot (c) shows the betatron tune vs the horizontal betatron amplitude, while the betatron tune at small betatron amplitude is 1.2777. By fitting the horizontal betatron tunes of the particles with different horizontal amplitudes, the nonlinear terms, which are also supporting the existence of the nonlinear detuning, are observed to be nonzero. When the horizontal betatron tune is moved to near $4\nu_x = 6$, four islands are clearly seen in Fig. 11(b). Plot (d) shows the horizontal betatron tune vs horizontal betatron amplitude, while the zero-amplitude tune is 1.4816. We notice that the horizontal tune of 1.5 is not a systematic second order resonance because the superperiod of the accelerator is 2, while $\nu_x = 1.5$ is a systematic fourth order resonance. The betatron tune of 1.25 is not a

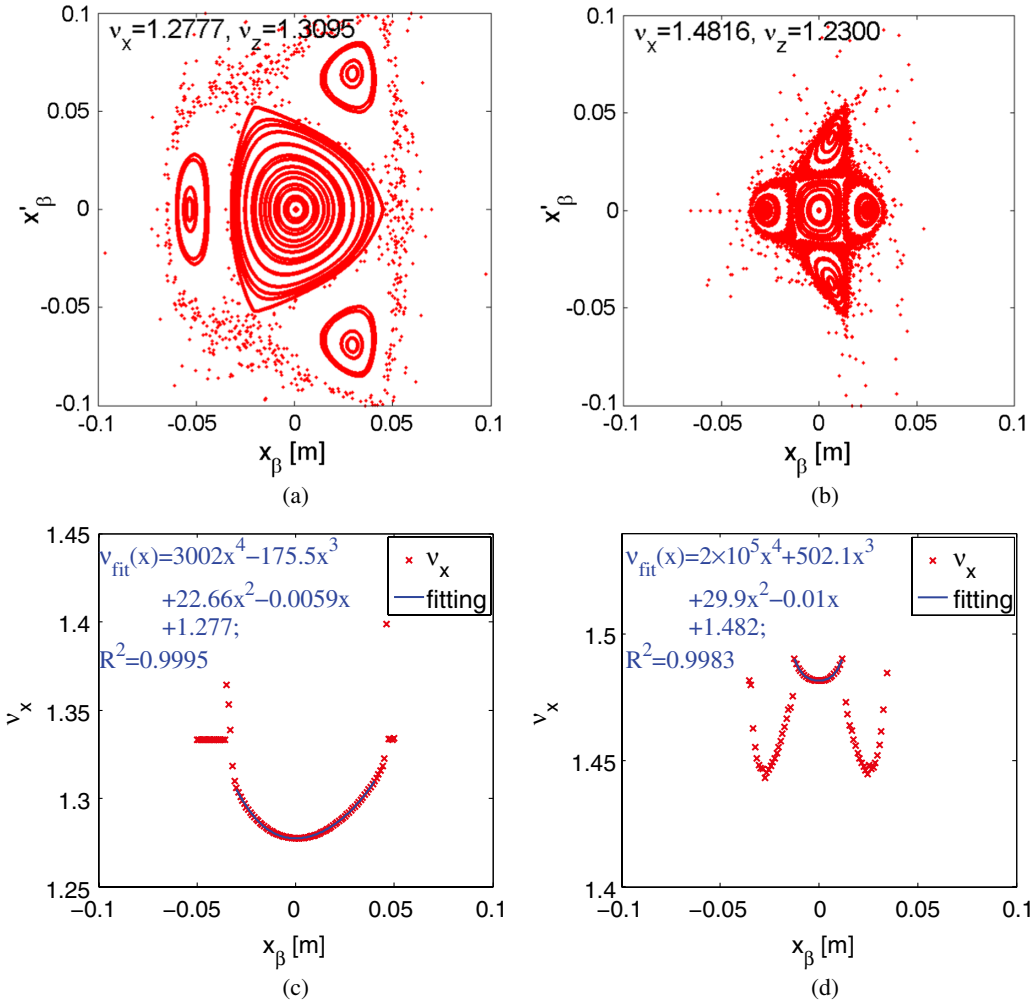

FIG. 11. Plot (a) shows the horizontal Poincaré surface of section at the $3\nu_x = 4$ resonance line. Plot (b) shows that of $4\nu_x = 6$ resonance line. Plots (c) and (d) show the dependence of the horizontal tune on the horizontal initial positions. The initial condition of other phase space coordinates are $x'_\beta = 0$, $z_\beta = 1 \times 10^{-5}$ m, and $z'_\beta = 0$.

systematic fourth order resonance, and does no harm to the dynamic aperture.

Nonlinear resonance and nonlinear detuning are key to the dynamic aperture. We have carefully chosen betatron tunes to achieve good dynamic aperture. This is the essential reason why we have increased the storage ring circumference from 3 to 4.8 meters or equivalently the dipole length from 0.22 to 0.40 m. For the 3.0 meter ring, the bending radius of the dipoles are about 0.14 m, and the effective nonlinear strength increases by a factor of 6. The dynamic aperture was too small for stable operation.

B. Multiparticle effects

The equilibrium beam parameters for electron storage rings depend mainly on synchrotron radiation damping, quantum excitation, intrabeam scattering (IBS), and residual gas scattering [35].

Electrons lose energy primarily along the direction of its motion due to synchrotron radiation while gaining energy from the rf cavity along the longitudinal direction. This effect results in damping in the 6D phase space. Since the photon emission is random and quantized, this quantum excitation gives rise to a finite beam emittance. The intrabeam scattering is small angle multiple Coulomb scattering between particles in a bunch, which causes beam emittance dilution [36,37]. Moreover, the multiple scattering from gas molecules inside the vacuum chamber can cause beam emittance dilution, too. We take the above effects into consideration and write down the equations of beam evolution [38]:

$$\frac{d\varepsilon_x}{dt} = -\frac{C_\gamma \mathcal{J}_x}{\rho T_0} E^3 \varepsilon_x + \frac{1}{C}\frac{3}{4}\langle \mathcal{H} \rangle_{\mathrm{dip}} \frac{C_u C_\gamma \hbar c^2 E^5}{(mc^2)^3 \rho^2} + 3.0636 \times 10^{-7} \times \frac{1}{E_k^2 + 2E_k E_0} P_g + \frac{2}{\tau_x}\varepsilon_x, \quad (11)$$

$$\frac{d\varepsilon_z}{dt} = -\frac{C_\gamma \mathcal{J}_z}{\rho T_0} E^3 (\varepsilon_z - \kappa \varepsilon_x) + \frac{1}{C}\frac{3}{4}\frac{1}{\gamma^2}\langle \beta_z \rangle_{\mathrm{dip}} \frac{C_u C_\gamma \hbar c^2 E^5}{(mc^2)^3 \rho^2} + 3.0636 \times 10^{-7} \times \frac{1}{E_k^2 + 2E_k E_0} P_g + \frac{2}{\tau_z}\varepsilon_z, \quad (12)$$

$$\frac{d\delta}{dt} = -\frac{C_\gamma \mathcal{J}_e}{2\rho T_0} E^3 \delta + \frac{1}{C}\frac{3}{8}\frac{C_u C_\gamma \hbar c^2 E^5}{(mc^2)^3 \rho^2 \delta} + 0 + \frac{1}{\tau_\delta}\delta, \quad (13)$$

where T_0 is the revolution period which is about 16 ns for the 4.8 m ring, C is the circumference of the ring, $C_u = 55/24\sqrt{3}$ is a constant, $C_\gamma = 4\pi r_0/[3(mc^2)^3] = 8.846 \times 10^{-5}$ m/(GeV)^3 is a quantum fluctuation constant for electrons, $E = 50$ MeV stands for the total energy of the reference particles, E_k and E_0 are the kinetic energy and rest energy of the electrons, $\rho = 0.2546$ m is the bending radius of the dipole magnets, $\langle \mathcal{H} \rangle_{\mathrm{dip}} = \frac{1}{2\pi\rho}\int_{\mathrm{dipole}} \mathcal{H} ds$ is the average $\mathcal{H}$ function in dipole magnets, $\langle \beta_z \rangle_{\mathrm{dip}}$ is the average vertical beta function in dipole magnets, κ is the emittance coupling constant, and P_g is the average pressure in the vacuum chamber. To provide realistic estimation, we use $P_g = 1$ nTorr. The horizontal, vertical, and longitudinal damping partition numbers, $\mathcal{J}_x$, $\mathcal{J}_z$, and $\mathcal{J}_e$ satisfy the Robinson theorem [39]. The growth time constant of IBS effect τ_x, τ_z, τ_δ are calculated from Bjorken and Mtingwa formalism [37] and are updated each step in time.

The first terms in Eqs. (11)–(13) stand for the synchrotron radiation damping effect. The second terms arise from the quantum excitation. The third terms are due to the residual gas scattering which produces a constant growth rate to the beam emittance if the vacuum is kept constant. The last terms are due to the IBS effect. Solving these emittance evolution equations, we obtain the equilibrium emittance and energy spread. The estimation of the equilibrium beam parameters are nontrivial because the IBS growth times (τ_x, τ_z, τ_δ) have to be updated as the beam intensity evolves.

However, the initial bunch length and momentum spread of the injected beam from linac are usually highly mismatched with the longitudinal equilibrium phase space in the ring. Due to the mismatch, the injected bunch will quickly filament in the synchrotron phase space. It is unrealistic to apply the above equilibrium evolution equations to the freshly injected beam. Thus we track the synchrotron motion of injected beam to reach a matched synchrotron phase space before solving the emittance evolution equations. Since the synchrotron period is about 50 turns, the synchrotron phase filamentation is very fast, of the order of 20 μs.

The Euler method [32] is applied to solve the evolution equations, in which the growth time constants of IBS effect in three directions are calculated by Bjorken-Mtingwa's model model [37]. However, one should notice that using the Bjorken-Mtingwa's model to calculate the growth time constants of IBS effect requires a Gaussian approximation of the beam's profile. As illustrated above, the distribution of an electron bunch changes dramatically during the beam filamentation process in the longitudinal phase space if the injected beam mismatches with the rf potential well. Since the filamentation takes place in the shorter time scale

TABLE II. The initial parameters of the injected beam in the longitudinal phase space.

Parameters	Values
Reference energy [MeV]	50
rms bunch length [ps]	10
rms momentum spread	0.5%

comparing to the time to achieve the state of equilibrium, we study the filamentation effect first. By applying the synchrotron mapping equations to all particles in the bunch turn by turn, a temporary state of equilibrium which matches with the rf potential well can be achieved. The distribution of the bunch after achieving the temporary matched state can be approximated as Gaussian distribution. The parameters of the beam at the temporary state of equilibrium can be used as the initial values in solving the evolution equations.

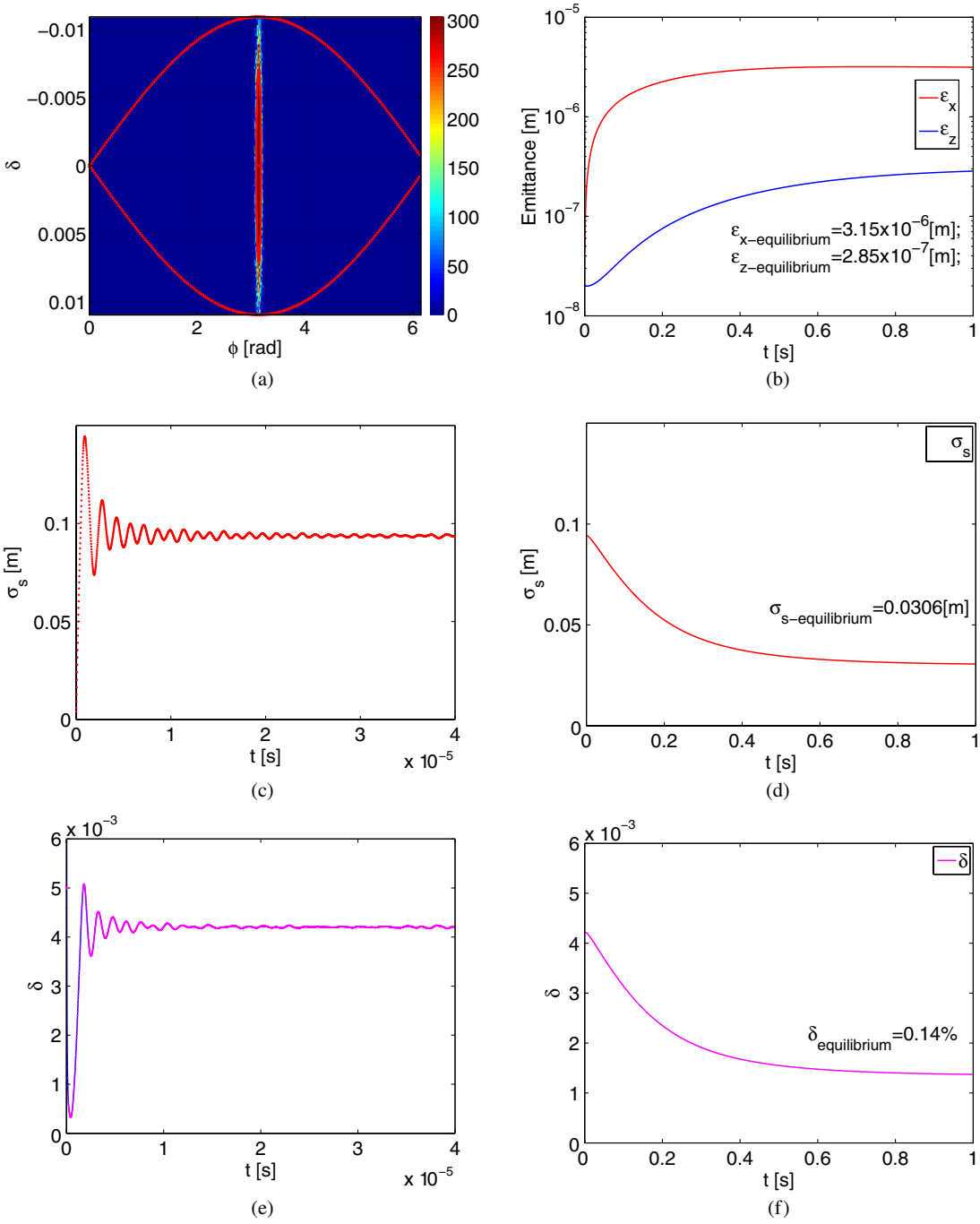

FIG. 12. The two-stage self-consistent simulation of the evolution of beam parameters from injection to the equilibrium. Part (a) shows the initial electron bunch in the longitudinal phase space following the parameters in Table II. It is highly mismatched with the rf bucket. The beam will filament in the bucket. The rms bunch length (c) and rms momentum spread (e) oscillate rapidly in the first thousands of turns and then reach a temporary "matched" state, which is claimed as the final situation of the first-stage simulation. Starting from this temporary matched state, Eqs. (11)–(13) are applied in the second-stage simulation. Plots (b), (d) and (f) show the evolution of transverse emittance, rms bunch length and rms momentum spread, respectively. We assume $\kappa = 0.1$ for 10% coupling.

We develop a two-stage self-consistent method to estimate the evolution of the beam parameters from injection to equilibrium. First, we generate macroparticles from the initial beam parameters in the linac and then track them in the longitudinal phase space by solving the synchrotron mapping equations until the electron bunch matches the rf potential well. Then we use the Euler method to solve the three evolution equations [Eqs. (11)–(13)] with the beam parameters of the temporary equilibrium as the initial values of equations. The electron beam is assumed to stay matched with the rf potential well in the process of solving the equations. The bunch length is updated at each time step.

Taking the peak rf voltage $V_{\rm rf} = 10$ kV as an example, we use the two stage code to simulate the beam evolution from the injection to equilibrium. A Gaussian beam, whose parameters are shown in Table II, is injected into the ring [shown in Fig. 12(a)] and start to tumble in the longitudinal bucket. The results of the first stage are shown in the Figs. 12(c) and 12(e) which correspond to the evolution of bunch length and momentum spread, respectively. As shown in these two plots, both bunch length and momentum spread oscillate violently before the temporary equilibrium state is achieved at about 2000 turns after the injection. The temporary equilibrium bunch length is about 310 ps (≈0.093 m), and the temporary equilibrium momentum spread is about 0.42%. The change of transverse emittances is neglected in the first stage because the time corresponding to 2000 turns is much shorter than the time needed to achieve the state of equilibrium with consideration of IBS, synchrotron radiation damping, quantum excitation, and residual gas scattering. The evolution of the transverse emittances, bunch length and momentum spread in the second stage are shown in Figs. 12(b), 12(d), and 12(f). It takes about 0.8 second to achieve the final equilibrium status in the second stage. The equilibrium horizontal emittance is about 3.15×10^{-6} m, meanwhile, the vertical one is about 2.85×10^{-7} m with 10% coupling between horizontal and vertical directions. Compare to the initial emittance (2.0×10^{-8} meter for both horizontal direction and vertical direction), the horizontal emittance increases more than 100 times while the vertical one increases about 10 times, both of which are dominated by IBS effect. The equilibrium bunch length is about 0.03 meter and the equilibrium momentum spread is 0.14%, which are shown in Figs. 12(d) and 12(f).

To be complete, we need to include the effects of electron-laser interaction in the calculation of the equilibrium beam parameters' evolution. The inverse Compton scattering has both damping effect and excitation effect [40] on the parameters of the electron beams. The laser's effects on the beam are treated as wiggler radiation. Both damping rate and excitation rate due to the ICS process are derived in Ref. [41]. The damping effects due to the ICS are expressed as

TABLE III. The parameters of laser pulses at the interaction point.

Parameters	Values
Laser wavelength λ_L [nm]	800
Energy E_L [mJ]	1
Duration σ_L [ps]	10
Spot size w_0 [μm]	50

$$\frac{d\varepsilon_x}{dt} = -\frac{\mathcal{J}_x U_0}{ET_0}\frac{\mu_0}{4\pi(\frac{1}{\rho}+\frac{1}{2\pi}\frac{\sigma_L}{\rho_L^2})}\frac{e^2}{p^2}\frac{P_{\rm laser}\sigma_s}{\pi c\sigma_x\sigma_z}\varepsilon_x, \tag{14}$$

$$\frac{d\varepsilon_z}{dt} = -\frac{\mathcal{J}_z U_0}{ET_0}\frac{\mu_0}{4\pi(\frac{1}{\rho}+\frac{1}{2\pi}\frac{\sigma_L}{\rho_L^2})}\frac{e^2}{p^2}\frac{P_{\rm laser}\sigma_s}{\pi c\sigma_x\sigma_z}\varepsilon_z, \tag{15}$$

$$\frac{d\delta^2}{dt} = -\frac{\mathcal{J}_e U_0}{ET_0}\frac{\mu_0}{4\pi(\frac{1}{\rho}+\frac{1}{2\pi}\frac{\sigma_L}{\rho_L^2})}\frac{e^2}{p^2}\frac{P_{\rm laser}\sigma_s}{\pi c\sigma_x\sigma_z}\delta^2, \tag{16}$$

where $P_{\rm laser}$ is the power of the laser pulse. σ_L is the duration of a laser pulse. ρ_L stands for the bending radius of the wiggler (laser). The emittance growth rates due to the ICS are

$$\frac{d\varepsilon_x}{dt} = \frac{1}{C}\frac{1}{2\pi}\mathcal{H}_{\rm IP}\frac{C_u C_\gamma \hbar c^2 E^5 e^3 B_L^3}{(mc^2)^3 p^3}\sigma_L, \tag{17}$$

$$\frac{d\varepsilon_z}{dt} = \frac{1}{C}\frac{1}{\gamma^2}\frac{1}{2\pi}(\beta_z)_{\rm IP}\frac{C_u C_\gamma \hbar c^2 E^5 e^3 B_L^3}{(mc^2)^3 p^3}\sigma_L, \tag{18}$$

$$\frac{d\delta^2}{dt} = \frac{1}{C}\frac{1}{2\pi}\frac{C_u C_\gamma \hbar c^2 E^5 e^3 B_L^3}{(mc^2)^3 p^3}\sigma_L, \tag{19}$$

where $\mathcal{H}_{\rm IP}$ is the invariant of the horizontal dispersion at the interaction point. $B_L = \sqrt{\frac{P_{\rm laser}\mu_0}{\pi\sigma_x\sigma_z c}}$ is the effective laser magnetic field.

By including the damping rate and excitation rate of ICS effect into the evolution equations, we estimate the new equilibrium beam parameters. The parameters of laser are shown in Table III. Our primary study shows that the influence of the ICS effect on the equilibrium beam parameters is negligible with the current parameters.

IV. OPTIMIZATION OF RF PARAMETERS AND THE X-RAY FLUX

In a low energy compact electron storage ring, the rf system determines not only the bunch length and momentum spread at the state of equilibrium but also the transverse emittance, mainly because of the IBS induced transverse-longitudinal coupling. To optimize the output x-ray flux, we should choose rf parameters carefully. Since we propose to use an existing 500 MHz reentrant-type normal

conducting cavity, only the rf voltage needs optimization. Qualitatively, the higher rf voltage results in the shorter bunch length, which may correspond to higher beam intensity. However, in the meantime, the transverse equilibrium emittance tend to be larger due to the stronger IBS effect, which tends to decrease the beam intensity. It is therefore difficult to determine the optimum rf voltage before calculating the equilibrium parameters and output x-ray flux in different cases. We estimate the total x-ray flux via the Monte-Carlo code CAIN [42].

Touschek lifetime is another limitation of the properties of the ring. The Touschek lifetime can be calculated by [43]

$$\frac{1}{\tau_{\text{Touschek}}} = \frac{N r_0^2 c}{8\pi\sigma_z\sigma_s\sigma_{x\beta}\sqrt{1+\sigma_{xs}^2/\sigma_{x\beta}^2}}\frac{\lambda^3}{\gamma^2}D(\xi), \quad (20)$$

where N is the number of particles in the electron bunch, $\sigma_{x\beta}$ and σ_{xs} are respectively the rms contributions to the horizontal beam size from the betatron and synchrotron motions, σ_z and σ_s stand for the vertical rms beam size and rms bunch length, respectively. The parameters λ, ξ and $D(\xi)$ are defined as

$$\frac{1}{\lambda} = \left(\frac{\Delta E}{E}\right)_{rf} = \frac{\epsilon_{rf}}{\gamma m_0 c},$$

$$\xi = \left(\frac{\epsilon_{rf}}{\gamma\sigma_p}\right)^2,$$

$$D(\xi) = \sqrt{\xi}\left\{-\frac{3}{2}e^{-\xi} + \frac{\xi}{2}\int_\xi^\infty \frac{\ln(u)e^{-u}}{u}du + \frac{1}{2}(3\xi - \xi\ln(\xi) + 2)\int_\xi^\infty \frac{e^{-u}}{u}du\right\},$$

where $\epsilon_{rf} = (2\nu_x/h\alpha_c)Y(\phi_s)$ is the rf bucket height.

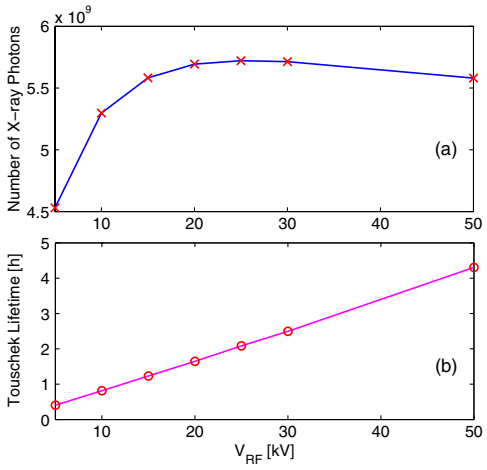

FIG. 13. (a) The x-ray flux at different V_{rf}. Part (b) shows the Touschek lifetime at different V_{rf}. The corresponding Touschek lifetime is about 2 hours when the maximum x-ray flux (about 5.7×10^9 photons/s) is achieved.

TABLE IV. The requirement of the parameters of the rf system.

Parameters	Values
Central frequency [MHz]	499.65
Work mode	cw
Power [W]	125
Cavity type	Normal conducting, reentrant type
Shunt impedance [MΩ]	≈5

We calculate the dependence of the Touschek lifetime on the peak rf voltage as shown in Fig. 13(b), which shows that the Touschek lifetime is longer than 1 hour when the peak rf voltage is higher than 10 kV.

Figure 13(a) shows that the x-ray flux increases dramatically when V_{rf} changes from 5 to 15 kV. After that it changes slowly and reaches a maximum value at about $V_{\text{rf}} \approx 25$ kV before decreasing gradually. Since the shunt impedance of our cavity is approximately 5 MΩ, the required input power is about 125 W, which is easily provided by a solid-state cw rf power source. In this case, the Touschek lifetime is approximately 2 hours. Some basic requirements of the rf system are summarized in Table IV.

V. CONCLUSION

In this paper, we illustrate the design strategy of compact low energy electron storage rings. We show that the edge angle of dipole magnets plays a key role in providing linear focusing to particles. Based on this strategy, we design a ring with the circumference of 4.8 meter for the Tsinghua Thomson scattering x-ray source. The basic lattice is made up of four 90 degree dipole magnets with 37° edge angle at both the entrances and the exits. Two quadrupole magnets are used to control the damping partition number. The momentum compaction factor can also be varied, e.g. from 1.1 to −0.5.

The intrinsic nonlinearity of the dipole magnets is found to be very important to dynamic aperture. The nonlinear potential is inversely proportional to the cubic of the bending radius. Our particle tracking results agree well with analytic analysis. Systematic third order and fourth order resonances are observed (see Fig. 11) by adjusting the bare tune closed to the $3\nu_x = 4$ and $4\nu_x = 6$ resonance lines, respectively.

Away from the resonances, we find that our lattice has excellent dynamic aperture for the particles with momentum spread from −3% to 3%. At the quadrupole strength of 3 m^{-1}, the operation lattice is a 2-double-bend achromat structure with two dispersion free straight sections. We apply the frequency map analysis to study the tune spread and tune diffusion rate of the beam with momentum spread inside the vacuum chamber region. An on-axis injection scheme is also designed.

A two-stage self-consistent method is developed to study the beam evolution process before reaching the state of equilibrium. The first stage corresponds to synchrotron phase space filamentation due to mismatch of linac bunch with that of the storage ring. This filamentation stage is very fast, because the synchrotron period is of the order of 50 turns. A temporary equilibrium in the longitudinal phase space is used as the initial condition of the second stage beam evolution, which includes IBS effect, synchrotron radiation damping, quantum excitation, and residual gas scattering. We use the Euler method to solve the emittance evolution equations. By calculating the equilibrium parameters under different peak rf voltage, the generated x-ray photon flux is optimized.

The estimated x-ray flux is about 5.7×10^9 photons/s in the current design, which is less than the design values in other similar projects. One reason is the energy of a laser pulse of 1 mJ used in our calculation is conservative. Moreover, we can optimize the x-ray flux further by reducing the betatron amplitudes at the interaction point.

We believe that the design of this small ring is interesting because there is a great amount of accelerator physics in this ring. This 4.8 m ring can provide good opportunity to explore accelerator physics on effects of momentum compaction factor on the dynamics, the dynamic aperture of accelerators with small bending radius, effects of edge angle, IBS, Touschek lifetime, electron-laser interaction, etc.

ACKNOWLEDGMENTS

This work is supported by the National Natural Science Foundation of China (Grants No. 10925523 and No. 11127507), S. Y. Lee is supported by the U.S. Department of Energy under Contract No. DE-FG02-12ER41800, and the National Science Foundation No. NSF PHY-1205431.

[1] P. Sprangle, A. Ting, E. Esarey, and A. Fisher, J. Appl. Phys. **72**, 5032 (1992).
[2] W. J. Brown and F. V. Hartemann, Phys. Rev. ST Accel. Beams **7**, 060703 (2004).
[3] O. Klein and Y. Nishina, Nature (London) **122**, 398 (1928).
[4] Z. Huang and R. D. Ruth, Phys. Rev. Lett. **80**, 976 (1998).
[5] R. J. Loewen, Ph.D. thesis, Stanford University, 2003.
[6] P. C. Yu, Y. Wang, and W. H. Huang, Phys. Rev. ST Accel. Beams **12**, 061301 (2009).
[7] A. Loulergue *et al.*, *Proceedings of the 1st International Particle Accelerator Conference (IPAC'10), Kyoto, Japan, 2010* pp. 4650–4652.
[8] J. Abendroth *et al.*, J. Struct. Funct. Genom. **11**, 91 (2010).
[9] See a book about the theory of synchrotron radiation, e.g. A. Hofmann, *The Physics of Synchrotron Radiation* (Cambridge University Press, Cambridge, England, 2004).
[10] A. Piwinski, in *Proceedings of the 4th Advanced Accelerator Physics Course, 1991* (CERN, Geneva, 1992), p. 226.
[11] M. Venturini, in *Proceedings of the 19th Particle Accelerator Conference, Chicago, Illinois, 2001* (IEEE, Piscataway, NJ, 2001), pp. 2958–2960.
[12] P. Gladkikh, Phys. Rev. ST Accel. Beams **8**, 050702 (2005).
[13] S. Y. Lee, J. Kolski, Z. Liu, X. Pang, C. Park, W. Tam, and F. Wang, Rev. Sci. Instrum. **78**, 075107 (2007).
[14] P. C. Yu *et al.*, Chin. Phys. C (Suppl. II) **33**, 151 (2009).
[15] http://www.lynceantech.com/technology.html.
[16] E. Bulyak *et al.*, Nucl. Instrum. Methods Phys. Res., Sect. A **487**, 241 (2002).
[17] E. Bulyak *et al.*, Nucl. Instrum. Methods Phys. Res., Sect. A **467–468**, 88 (2001).
[18] A. Variola *et al.*, Report No. LAL RT 09/28.
[19] V. Androsov *et al.*, *Proceedings of the 4th International Particle Accelerator Conference (IPAC'2013), Shanghai, China, 2013* pp. 225–227.
[20] V. Androsov *et al.*, *Proceedings of the 4th International Particle Accelerator Conference (IPAC'2013), Shanghai, China, 2013* pp. 2253–2255.
[21] C. X. Tang *et al.*, Nucl. Instrum. Methods Phys. Res., Sect. A **608**, S70 (2009).
[22] M. Berz, B. Erdélyi, and K. Makino, Phys. Rev. ST Accel. Beams **3**, 124001 (2000).
[23] K. L. Brown, Report No. SLAC-75, 1982.
[24] J. S. Kolski *et al.*, Report No. LA-UR-11-10334, 2011.
[25] S. Y. Lee, *Accelerator Physics* (World Scientific, Singapore, 2012).
[26] A. W. Chao, *Physics of Collective Beam Instabilities in High Energy Accelerators* (Wiley, New York, 1993).
[27] A. Nadji *et al.*, *Experiments with low and negative momentum compaction factor with Super-ACO, Proceedings of the Fifth European Particle Accelerator Conference (EPAC'96), Sitges (Barcelona), 1996*, (Institute of Physics, Bristol, 1996) p. 676.
[28] J. Laskar and D. Robin, *Proceeding of the 2nd International Workshop on Single Particle Eects in Large Hadron Colliders, Montreux, Switzerland, 1995*, pp. 183–192.
[29] M. Borland, Advanced Photon Source Report No. LS-287, 2000.
[30] H. S. Xu, W. H. Huang, and C. X. Tang, Rev. Sci. Instrum. **85**, 033305 (2014).
[31] CST (Computer Simulation Technology) EM STUDIO, http://www.cst.com.
[32] J. C. Butcher, *Numerical Methods for Ordinary Differential Equations* (John Wiley & Sons, New York, 2003), ISBN 978-0-471-96758-3.
[33] D. Alesini *et al.*, Report No. EUROTeV-Report-2006-025, 2006.
[34] T. Naito *et al.*, *Proceedings of the 22nd Particle Accelerator Conference, Albuquerque, New Mexico, 2007* (IEEE, New York, 2007), pp. 2272–2774.
[35] T. H. Luo, Ph.D. thesis, Indiana University, 2011.
[36] A. Piwinski, *Intra-beam scattering, Proceedings of the 9th International Conference on High-Energy Accelerators, SLAC, Stanford, CS, USA, 1974*, pp. 405–409.

[37] J. D. Bjorken and S. K. Mtingwa, *Part. Accel.* **13**, 115 (1983).
[38] H. S. Xu *et al.*, *Proceedings of the 4th International Particle Accelerator Conference (IPAC 2013), Shanghai, China, 2013* pp. 1625–1627.
[39] K. Robinson, Phys. Rev. **111**, 373 (1958).
[40] Z. Huang, Report No. SLAC-R-527, 1998.
[41] T. H. Luo, Y. C. Jing, and S. Y. Lee, Internal Report, Indiana University, 2010.
[42] P. Chen *et al.*, Report No. SLAC-PUB-6583, 1994.
[43] J. Le Duff, *Proceedings of the 5th Advanced Accelerator Physics Course, "CAS-CERN Accelerator School" Rhodes, Greece, 1993*, pp. 573–586.